frontiers in Chemistry

ORIGINAL RESEARCH
published: 20 March 2018
doi: 10.3389/fchem.2018.00069

Self-Propagating Combustion Synthesis, Luminescent Properties and Photocatalytic Activities of Pure $Ca_{12}Al_{14}O_{33}$: Tb^{3+}(Sm^{3+})

Rong Liu[1]*, *Yongsheng Yan*[2] *and Changchang Ma*[2]

[1] School of Chemistry, BaiCheng Normal University, Baicheng, China, [2] Institute of Green Chemistry and Chemical Technology, Jiangsu University, Zhenjiang, China

The dual-functional $Ca_{12}Al_{14}O_{33}$: Tb^{3+} and $Ca_{12}Al_{14}O_{33}$: Sm^{3+} materials were prepared by the Self-Propagating Combustion Synthesis (SPCS) technology. The structure, morphology and light absorption property were investigated by XRD, FT-IR, UV-Vis DRS and SEM etc. The doping of Tb^{3+} and Sm^{3+} ions had not changed cubic structure of $Ca_{12}Al_{14}O_{33}$ but leaded to the slight lattice dilatation and the red-shifts of absorption peaks/edges. The excitation and emission spectra indicated that $Ca_{12}Al_{14}O_{33}$: Tb^{3+} and $Ca_{12}Al_{14}O_{33}$: Sm^{3+} are superior green and red luminescent materials, respectively, and it displayed the distinctly refined structure characteristics which had importantly reference value for the energy level investigation of Tb^{3+} and Sm^{3+} ions. Meanwhile, $Ca_{12}Al_{14}O_{33}$: Tb^{3+} and $Ca_{12}Al_{14}O_{33}$: Sm^{3+} also exhibited the improved photocatalytic degradation for removing dye MB compared with bare $Ca_{12}Al_{14}O_{33}$.

Keywords: SPCS, $Ca_{12}Al_{14}O_{33}$: Tb^{3+}(Sm^{3+}), pure phase, luminescent property, photocatalytic activity

OPEN ACCESS

Edited by:
Pellegrino Musto, Consiglio Nazionale Delle Ricerche (CNR), Italy

Reviewed by:
Omkar Singh Kushwaha, National Chemical Laboratory (CSIR), India
Ji-Jun Zou, Tianjin University, China

***Correspondence:**
Rong Liu
liurong63@126.com

Specialty section:
This article was submitted to Polymer Chemistry, a section of the journal Frontiers in Chemistry

Received: *16 September 2017*
Accepted: *05 March 2018*
Published: *20 March 2018*

Citation:
Liu R, Yan Y and Ma C (2018) Self-Propagating Combustion Synthesis, Luminescent Properties and Photocatalytic Activities of Pure $Ca_{12}Al_{14}O_{33}$: Tb^{3+}(Sm^{3+}). Front. Chem. 6:69. doi: 10.3389/fchem.2018.00069

INTRODUCTION

In recent years, the widespread application of rare-earth luminescent materials (RELMs) has been proved to promote the upgrading of products in display area (Yang et al., 2001; Xie et al., 2002; Zhang et al., 2017). RELMs have been a kind of essential materials in energy-efficient lighting and electronic information industry owing to their low-cost, good color display, pollution-free, long-life, nontoxic advantages and so on (Li et al., 2009; Yu et al., 2009). In addition, RELMs are widely used in agriculture, environmental sanitation, medical care, simulate natural light source, etc. special application fields (Li and Lin, 2010; Gai et al., 2014; Escudero et al., 2016, 2017).

It is always the intensive research subject to explore the novel oxide and composite oxide RELMs with high luminescent efficiency and favorable thermal stability. Especially, the RELMs based on alkaline-earth metal aluminates composite oxides have become the research focus due to their unique advantages of high luminescent efficiency, stable chemical properties, high quenching temperature, corrosion resistance, low-cost and nontoxic, pollution-free characteristics (Feng et al., 2010; Yu et al., 2013; Min et al., 2014). For example, high-efficiency green $MgAl_{11}O_{19}$: Ce^{3+}, Tb^{3+} (Jung et al., 2005) and blue $BaMgAl_{10}O_{17}$: Eu^{2+} (Kim et al., 2002) luminescent powders used Mg(Ba)O-Al_2O_3 as hosts had widely been applied in the world. Also, there are many reports on the blue-luminescent materials using SrO-Al_2O_3 system as hosts, including $Sr_2Al_6O_{11}$ (Takeda et al., 2002), $Sr_4Al_{14}O_{25}$ (Garcia et al., 2016), $SrAl_2O_4$ (Sohn et al., 2002), and $SrAl_4O_7$ (Singh et al., 2016), etc., as well as red-luminescent materials using $LiAlO_2$

(Lee et al., 2012), $LiAl_5O_8$ (Singh and Rao, 2008), and $CaAl_{12}O_{19}$ (Brik et al., 2011) as hosts. However, many of above materials are prepared by the traditional solid phase calcined method, which has the obvious deficiency of energy consumption because of high synthesis temperature. Especially for calcium aluminate host materials, they are difficult to obtain pure phase product owing to generation of many phases together in the preparation. Existence of mixed phases may influence on luminescence performance of RELMs when they are used as host materials. Therefore, in this paper, two pure phase RELMs using $Ca_{12}Al_{14}O_{33}$ as host material and Tb^{3+}(Sm^{3+}) as active ions are successful prepared by a simple SPCS technique. The synthesis temperature is significantly reduced. It is worth noting that both of $Ca_{12}Al_{14}O_{33}$: Tb^{3+} and $Ca_{12}Al_{14}O_{33}$: Sm^{3+} exhibit dual-functional features, not only show outstanding luminescent properties but also disply superior photocatalytic activities, which may have potential application prospects in display and catalysis fields.

EXPERIMENTAL

$Al(NO_3)_3{\cdot}9H_2O$, $Ca(NO_3)_2{\cdot}4H_2O$, urea and concentrated nitric acid are analytical reagent. The purity of Tb_4O_7 and Sm_2O_3 were ≥99.9%. The reaction materials were weighted making use of electronic balance in accordance with $Ca_{12-x}Al_{14}O_{33}$: $xTb^{3+}(Sm^{3+})$ (x = 0.01–0.05) stoichiometric ratio, respectively. The appropriate ratio Tb_4O_7 and Sm_2O_3 were transferred to 100 ml beakers and dissolved via a little concentrated HNO_3 (A.R.), respectively. After evaporating to dryness, $Al(NO_3)_3{\bullet}9H_2O$, $Ca(NO_3)_2{\bullet}4H_2O$, $CO(NH_2)_2$ and appropriate distilled water were added. Keeping on stirring, dissolving and heating until the solution was evaporated to be viscous, Subsequently, the beaker was put into a muffle furnace at 500°C. After a few minutes, the reaction material burned quickly and emited a bright flame. The entire combustion process was completed within 5–7 min. The white mushroom-shaped precursors with loose, porous and soft property were obtained. Finally, the precursors were grinded 30 min and transferred into the corundum crucible and calcined in the muffle furnace at 1,100°C for 6 h to obtain white products.

X-ray powder diffraction (XRD) patterns of products were recorded on Rigaku Dmax-2200 powder diffractometer (Cu $K_{\alpha1}$ = 1.54056 × 10^{-10} m, scanning speed 6° min^{-1}, scanning 2θ range 3–80° with steps of 0.02°). Luminescent spectra were measured via F4500 fluorescence spectrophotometer using Xe lamp as the excitation source (EX slit 2.5 nm/EM slit 2.5 nm, scanning speed 12,000 nm min^{-1}). Morphologies were observed with S-3000N scanning electron microscopy (SEM). All the measurements were carried out at room temperature. FT-IR absorption spectra were measured on FT-IR360 infrared spectrometer using KBr pellets in the region of 4,000–400 cm^{-1}. The UV-vis diffuse reflectance spectra (DRS) of the samples were recorded on a UV–vis spectrophotometer (PG, TU-1900) with $BaSO_4$ as the background at room temperature.

The dye methylene blue (MB) solution (10 mg L^{-1}, 100 ml) containing 0.1 g sample was irradiated under the UV-Visible light with a 300 W Xe arc lamp. Before the irradiation, it was stirred for 30 min in the dark to achieve the adsorption-desorption equilibrium between dye MB and sample. The absorbance of dye MB solution was monitored by UV-vis spectrophotometer (PG, TU-1901) every 5 min.

RESULTS AND DISCUSSION

Structure Analysis of the As-Prepared Samples

Figure 1 shows the X-ray powder diffraction (XRD) patterns of $Ca_{12}Al_{14}O_{33}$, $Ca_{12}Al_{14}O_{33}$: Tb^{3+} and $Ca_{12}Al_{14}O_{33}$: Sm^{3+}. All diffraction patterns accord with JCPDS PDF#09-0413 cards well. No other miscellaneous diffraction peaks are observed, which proves that the three samples are completely transformed into $Ca_{12}Al_{14}O_{33}$ crystalline phase without generating other types of calcium aluminates. Meanwhile, the sharp and intense diffraction peaks indicate that the as-prepared samples have high crystalline. We used PowderX (Dong, 1999) to execute smooth, deduct back bottom, and isolate $K_{\alpha2}$ line diffraction peak of Cu target, seek peak and perform the index treatment of each diffraction peak for the obtained XRD patterns. The results demonstrate that crystal cells of $Ca_{12}Al_{14}O_{33}$: Tb^{3+} and $Ca_{12}Al_{14}O_{33}$: Sm^{3+} belong to the cubic crystal system with an I-43d space group, and the crystal cell parameters are a = 11.9895 Å and a = 11.9892 Å, Z = 2, respectively. The crystal cell parameters of two samples are slightly bigger than that of $Ca_{12}Al_{14}O_{33}$ (11.9820 Å), which means that lattice mild expansion takes place after a small amount of Tb^{3+} or Sm^{3+} ions entering the crystal lattice to replace Ca^{2+} ions in $Ca_{12}Al_{14}O_{33}$.

FT-IR Absorption Spectra of the As-Prepared Samples

The fourier transforming infrared (FT-IR) absorption spectra of $Ca_{12}Al_{14}O_{33}$, $Ca_{12}Al_{14}O_{33}$: Tb^{3+} and $Ca_{12}Al_{14}O_{33}$: Sm^{3+} are shown in **Figure 2** which are basically coincide with the results of the reported $Ca_{12}Al_{14}O_{33}$ (Tas, 1998). The absorption band

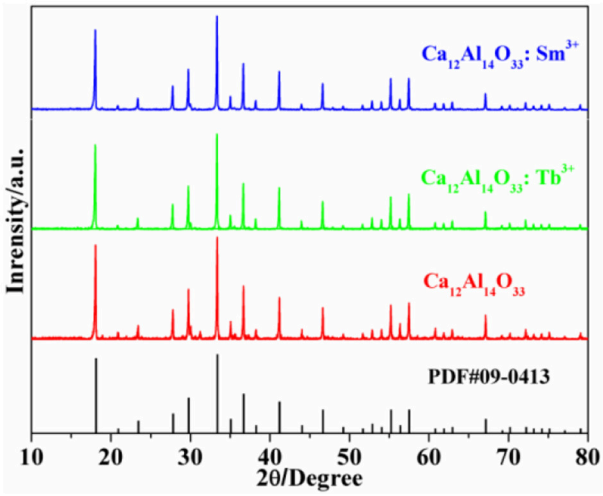

FIGURE 1 | XRD patterns of the as-prepared samples.

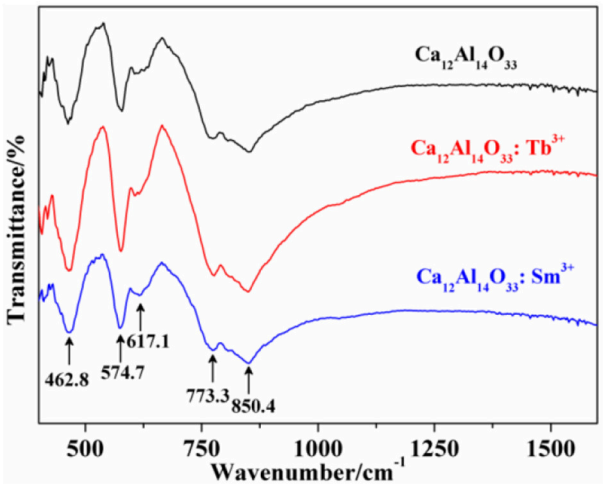

FIGURE 2 | FT-IR absorption spectra of the as-prepared samples.

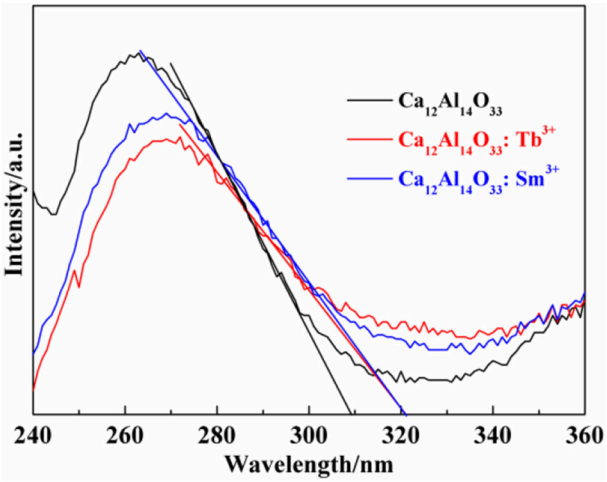

FIGURE 3 | UV-Vis DRS spectra of the as-prepared samples.

of condensate and isolation AlO_4 locates at the range of 900–700 cm^{-1} and 800–650 cm^{-1}, as well as the absorption band of condensate and isolation of AlO_6 locates at the range of 680–500 and 530–400 cm^{-1}, respectively (Yi et al., 2015). As a consequence, the strong broad band absorptions at around 800 cm^{-1} in **Figure 2** are attributed to AlO_4 stretching vibration, which are composed by two absorption peaks at 850.40 and 773.4 cm^{-1}. Those results demonstrate there are two AlO_4 tetrahedral structures in the lattice, which is accordance with the obtained structure in the $Ca_{12}Al_{14}O_{33}$ unit cell (Boysen et al., 2007). Because AlO_6 octahedral structure is inexistence in the $Ca_{12}Al_{14}O_{33}$ unit cell and the absorption band located at 400–620 cm^{-1} shows two group strong peaks in $Ca_3Al_2O_6$, $Ca_{12}Al_{14}O_{33}$, $CaAl_{12}O_{19}$, $CaAl_4O_7$, $CaAl_2O_4$, etc. calcium aluminate, the peaks located 617.1, 574.71, and 462.8 cm^{-1} should derive from characteristic vibration absorption of Al-O bonds. All the above prove that $Ca_{12}Al_{14}O_{33}$ crystal lattice structure is no more obviously changed except only slight distortion when the Ca^{2+} ions are replaced by Tb^{3+} or Sm^{3+}, which is consistent with XRD analysis results.

UV–Vis DRS of the As-Prepared Samples

The light absorption ability of the as-prepared samples is evaluated by the UV-vis diffuse reflectance spectra (DRS). As shown in **Figure 3** all samples exhibit strong ultraviolet light absorption characteristics located at 240–320 nm. The steep shapes indicate that the intense absorptions are not due to the transition from the impurity level but band-gap transition (Li et al., 2015, 2017). It is noted that the absorption peak and absorption edge of pure $Ca_{12}Al_{14}O_{33}$ are located at 263 nm and 309 nm, respectively. However, after doping Tb^{3+} and Sm^{3+} ions, the absorption peaks and absorption edges of $Ca_{12}Al_{14}O_{33}$: Tb^{3+} and $Ca_{12}Al_{14}O_{33}$: Sm^{3+} have apparent red-shift compared with that of original $Ca_{12}Al_{14}O_{33}$ sample, which is red-shift of about 6 and 12 nm toward the longer wavelengths and located at 269 and 321 nm, respectively. The optical absorption change may result from the doping effect of $Tb^{3+}$and Sm^{3+} causing slight lattice expansion of $Ca_{12}Al_{14}O_{33}$.

SEM Images of the As-Prepared Samples

The morphologies of the as-prepared samples are observed by photomicrographs measured via scanning electron microscopy (SEM). As shown in **Figures 4a–c** the images with low magnification of $Ca_{12}Al_{14}O_{33}$, $Ca_{12}Al_{14}O_{33}$: Tb^{3+} and $Ca_{12}Al_{14}O_{33}$: Sm^{3+} present porous and irregular bulk feature, which have the obvious agglomeration gathered by some particles. It may result from high-temperature calcination for a long time. Correspondingly, **Figures 4a1–c1** are the high-magnification SEM images of $Ca_{12}Al_{14}O_{33}$, $Ca_{12}Al_{14}O_{33}$: Tb^{3+} and $Ca_{12}Al_{14}O_{33}$: Sm^{3+}, respectively. Those samples exhibit honeycomb distribution composed of crystalline granular adhesions with few microns, smooth surface and better crystallization effect. This result can be attributed to the following reasons: in the SPCS process, a lot of gases are released to damage the formation of massive structures owing to urea burning, so that crystal nuclei growth is along to direction to formation of sphere shapes containing the lower surface energy. The shapes of as-prepared samples influence the luminescence performance to some extent and lots of researches have shown spherical surface are conducive to enhancing luminescent intensity (Kang et al., 2000).

Luminescent Properties of the As-Prepared Samples

The bare $Ca_{12}Al_{14}O_{33}$ has no luminescence property without doping earth ions. However, when $Ca_{12}Al_{14}O_{33}$ is doped by Tb^{3+} and Sm^{3+} ions, it will produce characteristic luminescent emission of these two ions. **Figure 5** is the luminescent emission intensity of $Ca_{12}Al_{14}O_{33}$: Tb^{3+} and $Ca_{12}Al_{14}O_{33}$: Sm^{3+} with different doping amount, where the standard of comparison is evaluated by the strongest energy level transition of $^5D_4 \rightarrow {}^7F_5$ for Tb^{3+} and $^4G_{5/2} \rightarrow {}^6H_{7/2}$ for Sm^{3+} ions. Obviously, the

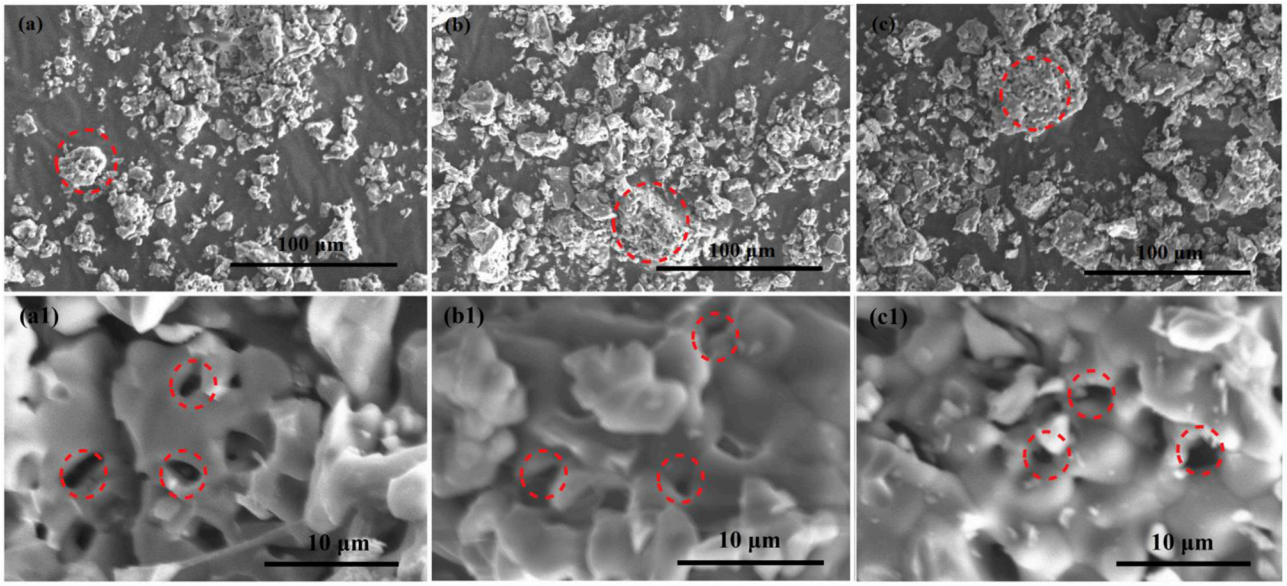

FIGURE 4 | SEM images of $Ca_{12}Al_{14}O_{33}$ **(a,a1)**, $Ca_{12}Al_{14}O_{33}$: Tb^{3+} **(b,b1)**, and $Ca_{12}Al_{14}O_{33}$: Sm^{3+} **(c,c1)** samples.

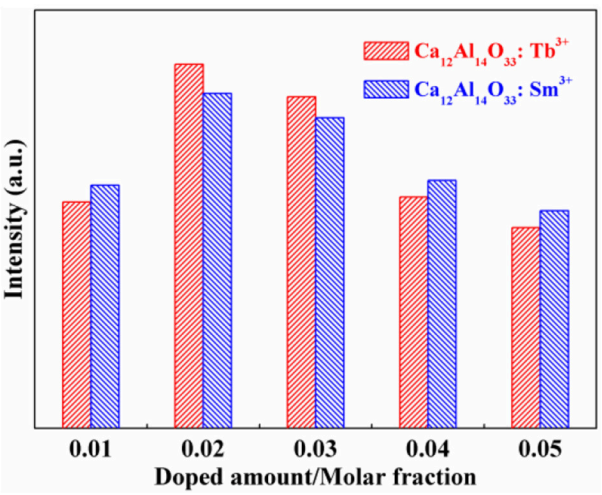

FIGURE 5 | Effect of doped amount on the luminescent intensity of the as-prepared samples.

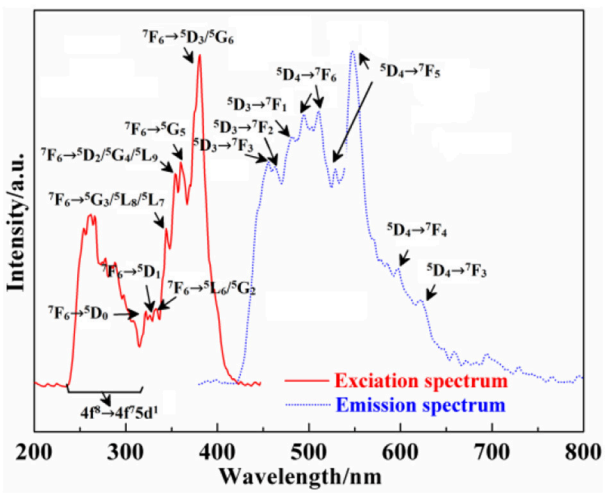

FIGURE 6 | Excitation and emission spectra of $Ca_{12}Al_{14}O_{33}$: Tb^{3+}.

luminescent intensity of $Ca_{12}Al_{14}O_{33}$: Tb^{3+} and $Ca_{12}Al_{14}O_{33}$: Sm^{3+} present increase first and then decrease with increasing the doping amount of Tb^{3+} and Sm^{3+} ions. When the doping amount of Tb^{3+} and Sm^{3+} is 0.02 of molar fraction, the luminescent emissions reach up the strongest intensity, because the excess rare earth ions usually produce fluorescence quenching effect that results in reduction of luminescent emission intensity.

Figure 6 shows the excitation (λ_{em} = 545 nm) and emission spectra (λ_{ex} = 359 nm) of $Ca_{12}Al_{14}O_{33}$: Tb^{3+}. Because the $4f^7$ state of Tb^{3+} ions has a stable semi-filled electron configuration, Tb^{3+} ions can be excited by the relative low energy, whose excitation band is always composed by f→ f and f→ d transition. Therefore, from the excitation spectrum of $Ca_{12}Al_{14}O_{33}$: Tb^{3+}, we can draw to a conclusion that the excitation band at the short-wave 220–315 nm corresponds to the $4f^8 \rightarrow 4f^7 5d^1$ transition absorption of Tb^{3+} ions, and the excitation band located at 320–400 nm originates from f→ f transition absorption, where the energy level transition of different absorption peaks at 381, 360, 354, 344, 333, 326, and 322 nm may be attributable to the energy level transition absorption of $^7F_6 \rightarrow$ ($^5D_3/^5G_6$), $^5G_5$, ($^5D_2/^5G_4/^5L_9$), ($^5G_3/^5L_8/^5L_7$), ($^7F_6 \rightarrow$ $^5L_6/^5G_2$), $^5D_1$, $^5D_0$, respectively (Fu et al., 2010). Furthermore, from the emission

spectrum of $Ca_{12}Al_{14}O_{33}$: Tb^{3+}, we can find that the common linear emission peak of Tb^{3+} ion presents wide band distribution, which is different from other common fluorescent materials (Fu et al., 2010; Dong, 2011). The emission peaks located at (495, 511), (529, 547), 597, and 623 nm come from the energy level transition of $^5D_4 \rightarrow {}^7F_6$, $^7F_5$, $^7F_4$, $^7F_3$, respectively (Fu et al., 2010). Due to the large *J*-value of the transition, the crystal field will result in the splitting of these energy levels. Meanwhile, to eliminate the parity-forbidden transition of Tb^{3+} ions, the opposite parity energy level of 4f configuration is not the charge transfer band, but is the $4f^7 5d^1$ energy level with low energy. $^5D_4 \rightarrow {}^7F_6$ electric dipole transition of Tb^{3+} ions is not as sensitive to ligand environment as the $^5D_0 \rightarrow {}^7F_2$ electric dipole transition of Eu^{3+} ions. Therefore, $^5D_4 \rightarrow {}^7F_5$ magnetic dipole transition is the strongest in the emission spectra, so that the $Ca_{12}Al_{14}O_{33}$: Tb^{3+} sample emits green light when it is excited under the ultraviolet light. Meanwhile, the stronger emission peaks located at 456, 463, and 482 nm origin from the higher excited states $^5D_3 \rightarrow {}^7F_3$, $^7F_2$, $^7F_1$ energy level transitions, respectively, which indicates that there is lightly cross relaxation between $^5D_3$ and $^5D_4$ energy levels (Fu et al., 2010; Dong, 2011).

Moreover, the excitation ($\lambda_{em} = 604$ nm) and emission spectra ($\lambda_{ex} = 382$ nm) of $Ca_{12}Al_{14}O_{33}$: Sm^{3+} are exhibited in **Figure 7** As can be seen from the excitation spectrum, there are five groups of excitation peaks in the range from 320 to 420 nm. It corresponds to the high energy f→ f configuration transition absorption of Sm^{3+} ions, where the excitation peaks located at 406, 379, 372, 367, and 348 nm may be belong to the transition absorption of $^6H_{5/2} \rightarrow$ ($^4F_{7/2}/^4L_{13/2}$),($^4D_{1/2}/^6P_{7/2}$),($^6H_{5/2} \rightarrow {}^4L_{17/2}/^4K_{13/2}$),$^4F_{9/2}$,$^4K_{15/2}$, respectively (Zhang et al., 2010). From the emission spectrum, the emission peaks located at 568 nm, 604 nm, 655 nm and 714 nm come from the energy level transition of $^4G_{5/2} \rightarrow {}^6H_{5/2}$, $^6H_{7/2}$, $^6H_{9/2}$, $^6H_{11/2}$, respectively (Zhang et al., 2010). P. S. May and coworkers (May et al., 1992) found that, $^4G_{5/2} \rightarrow {}^6H_{5/2}$ mainly belongs to a magnetic dipole transition, and partly belongs to electric dipole transition; though $^4G_{5/2} \rightarrow {}^6H_{7/2}$ is magnetic dipole transition, the electric dipole transition plays a predominance function; $^4G_{5/2} \rightarrow {}^6H_{9/2}$ is assigned to electric dipole transition, but the magnetic dipole transition is forbidden. In addition, according to the results reported by Tamura (Tamura and Shibukawa, 1993), if Sm^{3+} ion mainly occupies the asymmetry center, it can produce typical emission near 650 nm. On the contrary, if Sm^{3+} ion mainly occupies the symmetry center, it can produce typical emission near 602 nm. Therefore, as can be seen from the emission spectrum of $Ca_{12}Al_{14}O_{33}$: Sm^{3+}, the transition emission intensity of $^4G_{5/2} \rightarrow {}^6H_{7/2}$ is bigger than that of $^4G_{5/2} \rightarrow {}^6H_{9/2}$, and the transition emission intensity of $^4G_{5/2} \rightarrow {}^6H_{5/2}$ is bigger than that of $^4G_{5/2} \rightarrow {}^6H_{9/2}$, which indicate the Sm^{3+} ions mainly occupies the symmetry center in the lattice. Besides, a strong and refined-structure transition emission peak is observed at 450–580 nm, which may come from the transition emission of high energy level of Sm^{3+} ions.

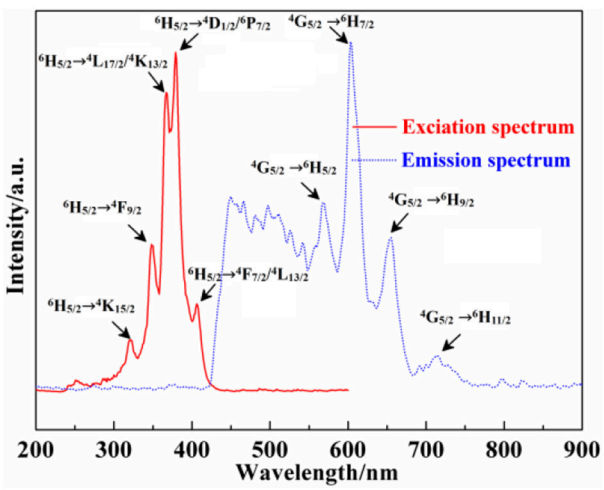

FIGURE 7 | Excitation and emission spectra of $Ca_{12}Al_{14}O_{33}$: Sm^{3+}.

Photocatalytic Activities of the As-Prepared Samples

The dye methylene blue (MB) is typical organic pollutant, which is usually used as target molecule to evaluate the photocatalytic ability of the photocatalytic materials (Dong et al., 2014c). **Figures 8A**, **9A** show the degradation dynamic curves of dye MB over the $Ca_{12}Al_{14}O_{33}$: Tb^{3+} and $Ca_{12}Al_{14}O_{33}$: Sm^{3+} samples, respectively. After running 15 min, two samples all show the high degradation rates is more than 98% for removing dye MB, respectively, whose photocatalytic activities are obviously higher than that of bare $Ca_{12}Al_{14}O_{33}$. Moreover, the kinetic curves of dye MB degradation can be approximated as the pseudo-first-order process (Dong et al., 2013, 2014a,b,c; Li et al., 2014, 2016). By plotting the $\ln(c_0/c)$ vs. time and making linear fitting for dynamic curves in **Figures 8B**, **9B** the removal rate constants (k) of dye MB are estimated to be 0.186 and 0.167 min^{-1}, respectively, which is distinctly higher than that of bare $Ca_{12}Al_{14}O_{33}$ (0.131 min^{-1}). Moreover, according to the absorbance variations of dye MB solutions in **Figures 8C**, **9C** in the photocatalytic reaction process, there are no shifting of the maximum absorption position of dye MB solution at 664 nm. In addition, the absorption peak at 293 nm in the ultraviolet range also vanishes, which implies that the benzene/heterocyclic rings of dye MB molecule may be completely decomposed, leading to the thorough mineralization of dye MB (Dong et al., 2013, 2014a,b,c; Li et al., 2014, 2016). Meanwhile, in order to investigate the reusability of the $Ca_{12}Al_{14}O_{33}$: Tb^{3+} and $Ca_{12}Al_{14}O_{33}$: Sm^{3+} samples, the circle degradation experiments of dye MB solution over the $Ca_{12}Al_{14}O_{33}$: Tb^{3+} and $Ca_{12}Al_{14}O_{33}$: Sm^{3+} samples are all performed. As shown in **Figures 8D**, **9D** the experimental results indicate the photocatalytic ability of two samples does not show obviously loss after four recycles, indicating that they have superior stability and reusability.

The Possible Luminescent and Photocatalytic Mechanism

The possible transfer behavior of charge carriers, luminescent emission and photocatalytic mechanism are shown in **Figure 10**

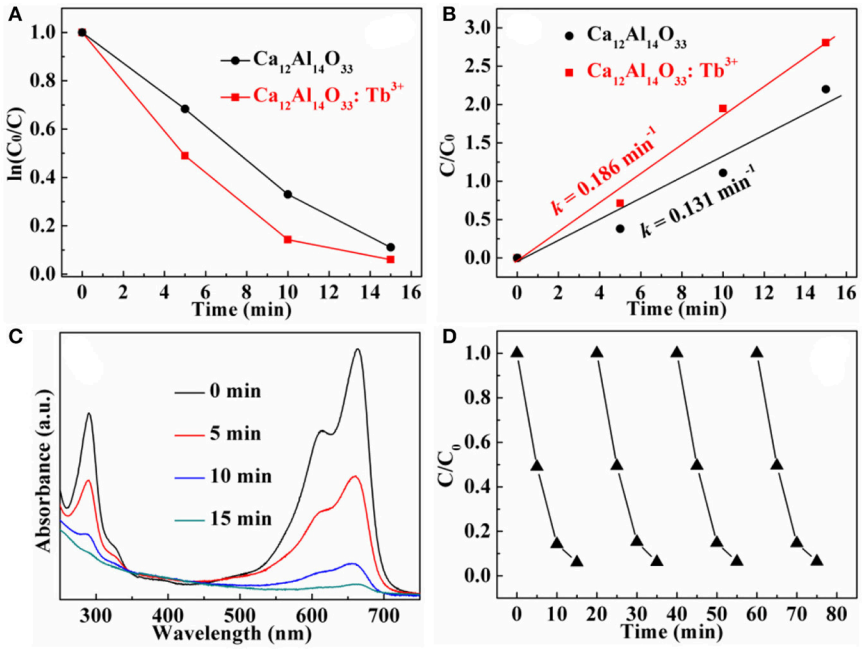

FIGURE 8 | Dynamic curves **(A)** and plots of ln(c_0/c) vs. time **(B)** of dye MB solution over $Ca_{12}Al_{14}O_{33}$ and $Ca_{12}Al_{14}O_{33}$: Tb^{3+}, absorbance variations **(C)** and cycle degradation runs **(D)** of dye MB solution over $Ca_{12}Al_{14}O_{33}$: Tb^{3+}.

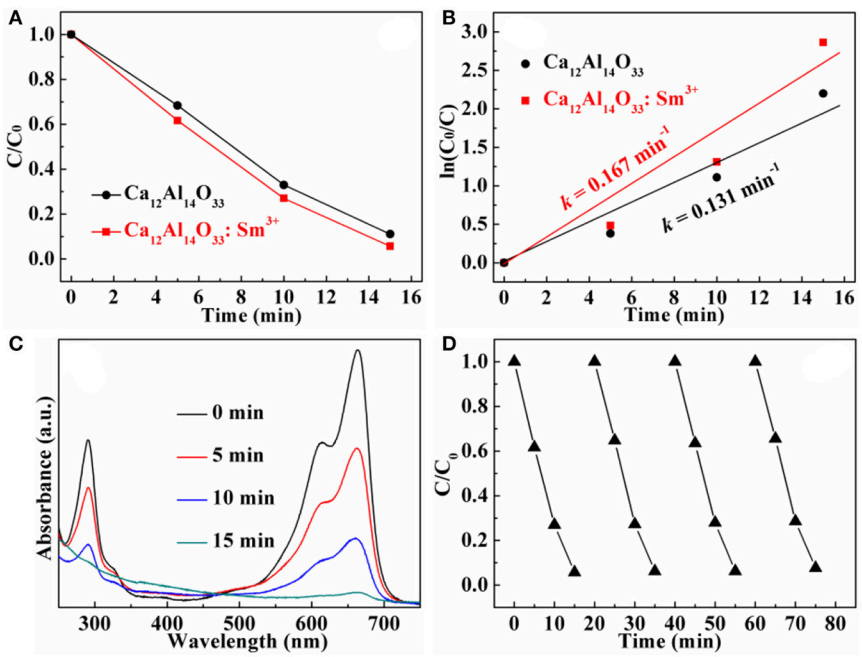

FIGURE 9 | Dynamic curves **(A)** and plots of ln(c_0/c) vs. time **(B)** of dye MB solution over $Ca_{12}Al_{14}O_{33}$ and $Ca_{12}Al_{14}O_{33}$: Sm^{3+}, absorbance variations **(C)** and cycle degradation runs **(D)** of dye MB solution over $Ca_{12}Al_{14}O_{33}$: Sm^{3+}.

Under the UV-vis light excitation, the $Ca_{12}Al_{14}O_{33}$ host and Tb^{3+} and Sm^{3+} ions are all excited at the same time. Electrons in the VB of $Ca_{12}Al_{14}O_{33}$ host transfer into the corresponding CB, as well as electrons in the ground state $^7F_6$ of Tb^{3+} and $^6H_{5/2}$ of Sm^{3+} ions transfer into the ($^5D_3$/$^5G_6$), $^5L_{10}$, $^5G_5$, ($^5D_2$/$^5G_4$/$^5L_9$), ($^5G_3$/$^5L_8$/$^5L_7$), ($^5L_6$/$^5G_2$), $^5D_1$, $^5D_0$ states and ($^4F_{7/2}$/$^4L_{13/2}$), ($^4D_{1/2}$/$^6P_{7/2}$), ($^4L_{17/2}$/$^4K_{13/2}$), $^4F_{9/2}$, $^4K_{15/2}$ states of them, respectively. At the luminescent process, the

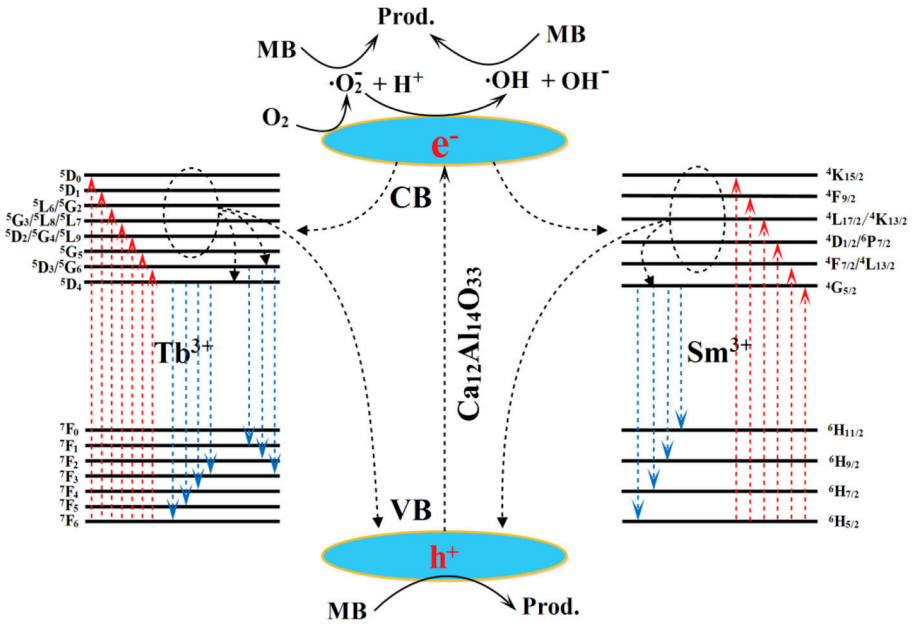

FIGURE 10 | The possible transfer behavior of charge carriers, luminescent emission and photocatalytic mechanism.

electrons in the excitation states $^5D_4$ and $^5D_3$ return to ^7F states of Tb^{3+} ions to generate luminescence, such as $^5D_4 \rightarrow {}^7F_6$, $^7F_5$, $^7F_4$, $^7F_3$ and $^5D_3 \rightarrow {}^7F_3$, $^7F_2$, $^7F_1$ transition emission. It should be pointed out that parts of electrons in the CB of $Ca_{12}Al_{14}O_{33}$ host and the high energy levels of Tb^{3+} can transfer into $^5D_4$ and $^5D_3$ states by means of multi-phonon assisted relaxation effect to enhance luminescent performance. Similarly, the electrons in the excitation state $^4G_{5/2}$ return to ^6H states of Sm^{3+} ions to generate luminescence, such as $^4G_{5/2} \rightarrow {}^6H_{5/2}$, $^6H_{7/2}$, $^6H_{9/2}$, $^6H_{11/2}$ transition emission. The parts of electrons in the CB of $Ca_{12}Al_{14}O_{33}$ host and the high energy levels of Sm^{3+} also can transfer into $^4G_{5/2}$ state by means of multi-phonon assisted relaxation effect to enhance luminescent performance. In the photocatalytic degrading MB process, parts of the electrons in the CB of the calcium aluminate host migrate to $Ca_{12}Al_{14}O_{33}$ host surface and are captured by O_2 molecules in water to yield superoxide radicals ($\bullet O_2^-$). The superoxide radicals may react with H^+ ions to further transform into hydroxyl radicals ($\bullet$OH). Finally, the superoxide radicals, hydroxyl radicals and holes all decompose MB dye molecules. In MB degradation process, the optical absorption increase may result from slight lattice expansion of $Ca_{12}Al_{14}O_{33}$ host owing to the doping effect of Tb^{3+} and Sm^{3+} ions, which may be the main reason for the improved photocatalytic performance.

CONCLUSIONS

The dual-functional $Ca_{12}Al_{14}O_{33}$: Tb^{3+} and $Ca_{12}Al_{14}O_{33}$: Sm^{3+} materials with single phase and good crystallinity are prepared by the SPCS technology. The investigation results indicate that there are no changes of cubic crystal structure after introducing Tb^{3+} or Sm^{3+} ions into $Ca_{12}Al_{14}O_{33}$ besides a slight lattice expansion. When the doping amount of Tb^{3+} and Sm^{3+} is 0.02 of molar fraction, both two samples show the maximum luminescent intensity. The excitation spectra of two samples are mainly from the f→ f transition absorption, and $Ca_{12}Al_{14}O_{33}$: Tb^{3+} sample also appears $4f^8 \rightarrow 4f^7 5d^1$ transition absorption at the short-wave region. In the emission spectra of two samples, the refined character emission can be observed, in which the transfer emissions of Tb^{3+} ions mainly come from $^5D_4 \rightarrow {}^7F_6$, $^7F_5$, $^7F_4$, $^7F_3$ and $^5D_3 \rightarrow {}^7F_3$, $^7F_2$, $^7F_1$, as well as the transfer emissions of Sm^{3+} ions come from $^4G_{5/2} \rightarrow {}^6H_{5/2}$, $^6H_{7/2}$, $^6H_{9/2}$, $^6H_{11/2}$ and high-energy transition emission at 450-580 nm, respectively. Meanwhile, two samples also exhibit the high photocatlytic degradation activity, stability and reusability for removing dye MB pollution. These two dual-functional materials may possess the potential application in the display device and dye wastewater treatment.

AUTHOR CONTRIBUTIONS

RL is in charge of synthesis and characterization of materials, and writing manuscript. YY is in charge of designing experimental plan and revising manuscript. CM is in charge of the performance test of materials.

ACKNOWLEDGMENTS

This work is financially supported by the National Natural Science Foundation of China (No. 21606114, 21407059 and 21407064).

REFERENCES

Boysen, H., Lerch, M., Styl, A., and Senyshyn, A. (2007). Structure and oxygen mobility in mayenite ($Ca_{12}Al_{14}O_{33}$): a high-temperature neutron powder diffraction study. *Acta Crystallogr. B* 63, 675–682. doi: 10.1107/S0108768107030005

Brik, M. G., Pan, Y. X., and Liu, G. K. (2011). Spectroscopic and crystal field analysis of absorption and photoluminescence properties of red phosphor $CaAl_{12}O_{19}$: Mn^{4+} modified by MgO. *J. Alloys Compd.* 509, 1452–1456. doi: 10.1016/j.jallcom.2010.11.117

Dong, C. (1999). PowderX: windows-95-based program for powder X-ray diffraction data procession. *J. Appl. Crystallogr.* 32:838. doi: 10.1107/S0021889899003039

Dong, H. (2011). Synthesis and luminescence properties of composite $CaAl_2O_4$-$2CaAl_4O_7$: Re^{3+} (Re=Tb, Sm) phosphors for application white LEDs. *J. Ceram. Process. Res.* 12, 704–707.

Dong, H., Chen, G., Sun, J., Feng, Y., Li, C., and Lv, C. (2014a). Stability, durability and regeneration ability of a novel Ag-based photocatalyst, $Ag_2Nb_4O_{11}$. *Chem. Commun.* 50, 6596–6599. doi: 10.1039/C4CC01183J

Dong, H., Chen, G., Sun, J., Feng, Y., Li, C., Xiong, G., et al. (2014b). Highly-effective photocatalytic properties and interfacial transfer efficiencies of charge carriers for the novel Ag_2CO_3/AgX heterojunctions achieved by surface modification. *Dalton Transac.* 43, 7282–7289, doi: 10.1039/C4DT00058G

Dong, H., Chen, G., Sun, J., Li, C., Yu, Y., and Chen, D. (2013). A novel high-efficiency visible-light sensitive Ag_2CO_3 photocatalyst with universal photodegradation performances: simple synthesis, reaction mechanism and first-principles study. *Appl. Catal. B Environ.* 134–135, 46–54. doi: 10.1016/j.apcatb.2012.12.041

Dong, H., Sun, J., Chen, G., Li, C., Hu, Y., and Lv, C. (2014c). An advanced Ag-based photocatalyst $Ag_2Ta_4O_{11}$ with outstanding activity, durability and universality for removing organic dyes. *Phys. Chem. Chem. Phys.* 16, 23915–23921, doi: 10.1039/C4CP03494E

Escudero, A., Becerro, A. I., Carrillo-Carrion, C., Nunez, N. O., Zyuzin, M. V., Laguna, M., et al. (2017). Rare earth based nanostructured materials: synthesis, functionalization, properties and bioimaging and biosensing applications. *Nanophotonics* 6, 881–921. doi: 10.1515/nanoph-2017-0007

Escudero, A., Carrillo-Carrión, C., Zyuzin, M. V., and Parak, W. J. (2016). Luminescent rare-earth-based nanoparticles: a summarized overview of their synthesis, functionalization, and applications. *Top. Curr. Chem.* 374:48. doi: 10.1007/s41061-016-0049-8

Feng, Z., Zhuang, W., Huang, X., Wen, X., and Hu, Y. (2010). Effect of MgF_2-H_3BO_3 flux on the properties of (Ce,Tb)$MgAl_{11}O_{19}$ phosphor. *J. Rare Earths* 28, 351–355. doi: 10.1016/S1002-0721(09)60110-1

Fu, C., Dong, H., Liu, C., and Wang, Y. (2010). Synthesis, structure and luminescence properties of phosphor $CaAl_2O_4$ activated by Tb^{3+}. *Optoelectronics Adv. Materials Rapid Commun.* 4, 73–76.

Gai, S., Li, C., Yang, P., and Lin, J. (2014). Recent progress in rare earth micro/nanocrystals: soft chemical synthesis, luminescent properties, and biomedical applications. *Chem. Rev.* 114, 2343–2389. doi: 10.1021/cr4001594

Garcia, C. R., Oliva, J., Romero, M. T., and Diaz-Torres, L. A. (2016). Enhancing the photocatalytic activity of $Sr_4Al_{14}O_{25}$: Eu^{2+}, Dy^{3+} persistent phosphors by codoping with Bi^{3+} ions. *Photochem. Photobiol.* 92, 231–237. doi: 10.1111/php.12570

Jung, D. S., Hong, S. K., Lee, H. J., and Kang, Y. C. (2005). Effect of boric acid flux on the characteristics of (CeTb)$MgAl_{11}O_{19}$ phosphor particles prepared by spray pyrolysis. *J. Alloys Compd.* 398, 309–314. doi: 10.1016/j.jallcom.2005.03.002

Kang, Y. C., Lenggoro, I. W., Park, S. B., and Okuyama, K. (2000). YAG: Ce phosphor particles prepared by ultrasonic spray pyrolysis. *Mater. Res. Bull.* 35, 789–798. doi: 10.1016/S0025-5408(00)00257-9

Kim, K. B., Kim, Y. I., Chun, H. G., Cho, T. Y., Jung, J. S., and Kang, J. G. (2002). Structural and optical properties of $BaMgAl_{10}O_{17}$:Eu^{2+} phosphor. *Chem. Mater.* 14, 5045–5052. doi: 10.1021/cm020592f

Lee, J. I., Pradhan, A. S., Kim, J. L., Chang, I., Kim, B. H., and Chung, K. S. (2012). Preliminary study on development and characterization of high sensitivity $LiAlO_2$ optically stimulated luminescence material. *Radiat. Meas.* 47, 837–840. doi: 10.1016/j.radmeas.2012.01.007

Li, C., Chen, G., Sun, J., Dong, H., Wang, Y., and Lv, C. (2014). Construction of Bi_2WO_6 homojunction via QDs self-decoration and its improved separation efficiency of charge carriers and photocatalytic ability. *Appl. Catal. B Environ.* 160–161, 383–389. doi: 10.1016/j.apcatb.2014.05.041

Li, C., Chen, G., Sun, J., Feng, Y., Liu, J., and Dong, H. (2015). Ultrathin nanoflakes constructed erythrocyte-like Bi_2WO_6 hierarchical architecture via anionic self-regulation strategy for improving photocatalytic activity and gas-sensing property. *Appl. Catal. B Environ.* 163, 415–423, doi: 10.1016/j.apcatb.2014.07.060

Li, C., Chen, G., Sun, J., Rao, J., Han, Z., Hu, Y., et al. (2016). Congmin Zhang Doping effect of phosphate in Bi2WO6 and universal improved photocatalytic activity for removing various pollutants in water. *Appl. Catal. B Environ.* 188, 39–47. doi: 10.1016/j.apcatb.2016.01.054

Li, C., Du, Y., Wang, D., Yin, S., Tu, W., Chen, Z., et al. (2017). Unique P-Co-N surface bonding states constructed on g-C_3N_4 nanosheets for drastically enhanced photocatalytic activity of H_2 evolution. *Adv. Funct. Mater.* 27:1604328. doi: 10.1002/adfm.201604328

Li, C., and Lin, J. (2010). Rare earth fluoride nano-/microcrystals: synthesis, surface modification and application. *J. Mater. Chem.* 20, 6831–6847. doi: 10.1039/c0jm00031k

Li, P., Peng, Q., and Li, Y. (2009). Dual-mode luminescent colloidal spheres from monodisperse rare-earth fluoride nanocrystals. *Adv. Mater.* 21, 1945–1948. doi: 10.1002/adma.200803228

May, P. S., Metcalf, D. H., Richardson, F. S., Carter, R. C., Miller, C. E., and Palmer, R. A. (1992). Measurement and analysis of excited-state decay kinetics and chiroptical activity in the transitions of Sm^{3+} in trigonal $Na_3[Sm(C_4H_4O_5)_3]\cdot 2NaClO_4\cdot 6H_2O$. *J. Lumin.* 51, 249–268. doi: 10.1016/0022-2313(92)90076-L

Min, X., Huang, Z., Fang, M., Liu, Y. G., Tang, C., and Wu, X. (2014). Energy transfer from Sm^{3+} to Eu^{3+} in red-emitting phosphor $LaMgAl_{11}O_{19}$:Sm^{3+}, Eu^{3+} for solar cells and near-ultraviolet white light-emitting diodes *Inorg. Chem.* 53, 6060–6065. doi: 10.1021/ic500412r

Singh, D., Tanwar, V., Simantilleke, A. P., Bhagwan, S., Mari, B., Kadyan, P. S., et al. (2016). Synthesis and enhanced luminescent characterization of $SrAl_4O_7$: Eu^{2+}, RE^{3+} (RE = Nd, Dy) nanophosphors for light emitting applications. *J. Mater. Sci.* 27, 5303–5308. doi: 10.1007/s10854-016-4428-2

Singh, V., and Rao, K. G. (2008). Studies of defects in combustion synthesized europium-doped $LiAl_5O_8$ red phosphor. *J. Solid State Chem.* 181, 1387–1392. doi: 10.1016/j.jssc.2008.03.007

Sohn, K. S., Seo, S. Y., Kwon, Y. N., and Park, H. D. (2002). Direct observation of crack tip stress field using the mechanoluminescence of $SrAl_2O_4$: (Eu, Dy, Nd). *J. Am. Ceram. Soc.* 85, 712–714. doi: 10.1111/j.1151-2916.2002.tb00158.x

Takeda, T., Takahashi, K., Uheda, K., Takizawa, H., and Endo, T. (2002). Crystal structure and luminescence properties of $Sr_2Al_6O_{11}$: Eu^{2+}. *J. Jpn Soc. Powder Powder Metallurgy* 49, 1128–1133. doi: 10.2497/jjspm.49.1128

Tamura, Y., and Shibukawa, A. (1993). Optical studies of CaS: Eu, Sm infrared stimulable phosphors. *Jpn. J. Appl. Phys.* 32, 3187–3196. doi: 10.1143/JJAP.32.3187

Tas, A. C. (1998). Chemical preparation of the binary compounds in the calcia-alumina system by self-propagating combustion synthesis. *J. Am. Ceram. Soc.* 81, 2853–2863. doi: 10.1111/j.1151-2916.1998.tb02706.x

Xie, R. J., Mitomo, M., Uheda, K., Xu, F. F., and Akimune, Y. (2002). Preparation and luminescence spectra of calcium- and rare - earth (R = Eu, Tb, and Pr)-codoped α-SiAlON ceramics. *J. Am. Ceram. Soc.* 85, 1229–1234. doi: 10.1111/j.1151-2916.2002.tb00250.x

Yang, P., Lu, M., Xu, D., Yuan, D., and Zhou, G. (2001). ZnS nanocrystals co-activated by transition metals and rare-earth metals - a new class of luminescent materials. *J. Lumin.* 93, 101–105. doi: 10.1016/S0022-2313(01)00186-7

Yi, L., Liu, X. Q., and Chen, X. M. (2015). Crystal structure and infrared reflection spectra of $SrLn_2Al_2O_7$ (Ln = La, Nd, Sm) microwave dielectric ceramics *Int. J. Appl. Ceram. Technol.* 12, E33–E40. doi: 10.1111/ijac.12366

Yu, D., Wu, Y., Liang, Y., Xia, Z., Zhang, M., and Yang, F. (2013). Sol-gel synthesis, growth mechanism and luminescence properties of uniform $Ce_{0.67}Tb_{0.33}MgAl_{11}O_{19}$ phosphor. *Powder Technol.* 246, 363–368. doi: 10.1016/j.powtec.2013.05.036

Yu, M., Li, F., Chen, Z., Hu, H., Zhan, C., Yang, H., et al. (2009). Laser scanning up-conversion luminescence microscopy for imaging cells labeled with rare-earth nanophosphors. *Anal. Chem.* 81, 930–935. doi: 10.1021/ac802072d

Zhang, X., Dong, H., and Mei, Z. (2010). Structure and luminescence properties of Sm^{3+} doped in $CaAl_2O_4$ phosphor. *Optoelectronics Adv. Mater. Rapid Commun.* 4, 28–32. wos: 000274804300007.

Zhang, X., Zhang, W., Li, Y., and Li, C. (2017). Hybrid luminescent materials of graphene oxide and rare-earth complexes with stronger luminescence intensity and better thermal stability. *Dyes Pigments* 140, 150–156. doi: 10.1016/j.dyepig.2017.01.019

Conflict of Interest Statement: The authors declare that the research was conducted in the absence of any commercial or financial relationships that could be construed as a potential conflict of interest.